Front. Environ. Sci. Eng. 2022, 16(12): 151
https://doi.org/10.1007/s11783-022-1586-8

RESEARCH ARTICLE

Cadmium removal mechanistic comparison of three Fe-based nanomaterials: Water-chemistry and roles of Fe dissolution

Xiaoge Huang[1], Lihao Chen[1], Ziqi Ma[1], Kenneth C. Carroll[2], Xiao Zhao (✉)[1], Zailin Huo[1]

1 College of Water Resources and Civil Engineering, China Agricultural University, Beijing 100083, China
2 Plant & Environmental Science Department, New Mexico State University, Las Cruces, NM 88003, USA

HIGHLIGHTS

- nZVI, S-nZVI, and nFeS were systematically compared for Cd(II) removal.
- Cd(II) removal by nZVI involved coprecipitation, complexation, and reduction.
- The predominant reaction for Cd(II) removal by S-nZVI and nFeS was replacement.
- A simple pseudo-second-order kinetic can adequately fit Fe(II) dissolution.

GRAPHIC ABSTRACT

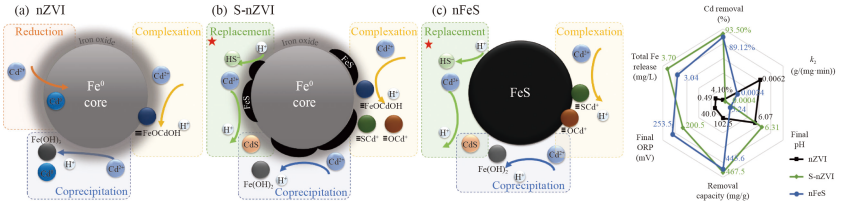

ARTICLE INFO

Article history:
Received 8 March 2022
Revised 6 May 2022
Accepted 8 May 2022
Available online 12 June 2022

Keywords:
Nano zero valent iron
Sulfided zero valent iron
FeS
Cd(II) immobilization
Fe dissolution

ABSTRACT

Cadmium (Cd) is a common toxic heavy metal in the environment. Taking Cd(II) as a target contaminant, we systematically compared the performances of three Fe-based nanomaterials (nano zero valent iron, nZVI; sulfidated nZVI, S-nZVI; and nano FeS, nFeS) for Cd immobilization under anaerobic conditions. Effects of nanomaterials doses, initial pH, co-existing ions, and humic acid (HA) were examined. Under identical conditions, at varied doses or initial pH, Cd(II) removal by three materials followed the order of S-nZVI > nFeS > nZVI. At pH 6, the Cd(II) removal within 24 hours for S-nZVI, nFeS, and nZVI (dose of 20 mg/L) were 93.50%, 89.12% and 4.10%, respectively. The fast initial reaction rate of nZVI did not lead to a high removal capacity. The Cd removal was slightly impacted or even improved with co-existing ions (at 50 mg/L or 200 mg/L) or HA (at 2 mg/L or 20 mg/L). Characterization results revealed that nZVI immobilized Cd through coprecipitation, surface complexation, and reduction, whereas the mechanisms for sulfidated materials involved replacement, coprecipitation, and surface complexation, with replacement as the predominant reaction. A strong linear correlation between Cd(II) removal and Fe(II) dissolution was observed, and we proposed a novel pseudo-second-order kinetic model to simulate Fe(II) dissolution.

1 Introduction

Large quantities of heavy metals are emitted into water, atmosphere, and soil, which is mainly due to human activities (mining, industrial waste-water discharge, sewage irrigation, etc.) and natural disasters (volcanic eruptions, torrential rains, earthquakes, etc.) (Ma and Gao, 2014). Studies revealed that cadmium (Cd) is one of the most toxic and commonly detected heavy metals in the environment. There are many Cd pollution problems in the world (Liu et al., 2011; Bi et al., 2013). For many years, polluted river water with cadmium concentrations up to even 4–8 mg/L were reported in Hunan, China (Wang et al., 2004). The seriously adverse effects of Cd on human health have been observed, including lung

✉ Corresponding author
E-mail: xiaozhao88@cau.edu.cn

impairment, hypertension, liver dysfunction, kidney damage, melanoma, and abnormal physiological development. According to WHO Guidelines for Drinking-water Quality, the maximum permissible concentration of Cd in drinking water is 0.003 mg/L (WHO, 2004). Thus, remediation of harmful heavy metal ions from water bodies is urgently needed.

In the context of water remediation, many materials and methods have been studied and applied for water treatment, including metal oxides (e.g. iron (Huang et al., 2013), manganese and/or aluminum oxides (Dong et al., 2000)), polymer modified silica (Thakur et al., 2017), carbon nanotubes (Li et al., 2003), and resins (Naushad et al., 2015). It has been shown recently that application of Fe-based nanomaterials can be an environmentally-friendly method for remediation of various pollutants, such as halogenated-organic compounds, nitroaromatic hydrocarbons, heavy metal cations, and oxyanions (He et al., 2007; Fu et al., 2015; He et al., 2018; Cai et al., 2020; Duan et al., 2020). Fe-based nanomaterials are cost effective with simplicity of application, and highly efficient for heavy metal treatment. Recently, three types of Fe-based nanomaterials were found to be effective on Cd(II) removal, including nanoscale zero-valent iron (nZVI) (Zhang et al., 2014; Su et al., 2015; Liang et al., 2020), sulfidated nanoscale zero-valent iron (S-nZVI) (Lv et al., 2018; Liang et al., 2020), and pyrites nanoparticles (nFeS) (Mustafa et al., 2010; Tian et al., 2020). A previous study reported that nZVI particles could achieve a removal capacity of 7.3 mg Cd(II)/ g nZVI (Li and Zhang, 2007). In another study, nZVI exhibited a high sorption capacity for Cd (66.9 mg Cd(II)/g nZVI), and this removal process reached equilibrium in less than 30 min (Zhang et al., 2014); Liang et al. had reported that S-nZVI had a high removal capacity for Cd (495 mg/g) (Liang et al., 2020), and Lv et al. also found a relatively large Cd removal capacity of 150 mg/g (Lv et al., 2018). Whereas, lower reported removal capacities for nFeS ranged from 13.4 mg Cd(II)/g (Mustafa et al., 2010) to 13.77 mg Cd(II)/g (Tian et al., 2020). All these nanomaterials have attracted much attention because of their high treatment efficiency, environmental friendliness, cost-effectiveness, and ease of application. As the effects of these Fe-based nanomaterials on Cd(II) removal have been extensively studied, it was important to compare these three nanomaterials systematically under the consistent conditions, which has not been done so far. Moreover, limited studies have focused on the relationship between the Fe(II) release and the removal of the contaminants to reveal the intrinsic reactivity of Fe-based materials. The Fe(II) release was determined without the presence of contaminants in some previous studies (Xie and Cwiertny, 2012; Li et al., 2015). However, the correlation between the Fe(II) dissolution and Cd(II) removal capacity under various conditions has not been evaluated. In addition, an appropriate kinetic model for Fe(II) release is needed for prediction and system design. Moreover, how sulfidation influences the correlation remains unknown.

The overall goal of this research was to systematically compare three Fe-based nanomaterials (nZVI, S-nZVI, and nFeS) for reductive immobilization of Cd(II) in groundwater under varied conditions. Specifically, this work aimed to: 1) test the influence of different dosages of these three nanoparticles for Cd(II) immobilization; 2) explore the effect of the different initial pH; 3) examine the effect of variability of groundwater chemistry typical conditions, such as co-existing (Na^+, Ca^{2+}, NO_3^-, and CO_3^{2-}) and Humid Acid; 4) comprehensively compare the reaction rate and pathway of these three materials based on characterization results; and 5) elucidate the underlying Cd(II) immobilization removal mechanisms and the role of Fe(II) dissolution. This comparison of these materials in terms of reactivity, stability, and pollutant removal capacity supports design and application of Fe-based nanotechnology for water treatment application.

2 Materials and methods

2.1 Chemicals

All chemicals are analytical grade or higher, and solutions are prepared with deionized water (18.25 MΩ·cm, EPED-PLUS-E2-20TH system, Nanjing Yipu Yida Co., Ltd Jiangsu, China). Fe sulfate heptahydrate ($FeSO_4·7H_2O$, 99.0%), and sodium borohydride ($NaBH_4$, ⩾ 98%) were obtained from Alfa Aesar (Ward Hill, MA, USA). Sodium hydroxide (NaOH, 98%), cadmium chloride ($CdCl_2$, 99%), sodium chloride (NaCl, 99.5%), and anhydrous calcium chloride ($CaCl_2$, ⩾ 96.0%) were obtained from Aladdin (Shanghai, China). Sodium sulfide nonahydrate ($Na_2S·9H_2O$, ⩾ 99.9%) was obtained from Macklin (Shanghai, China). Anhydrous sodium carbonate (Na_2CO_3, 99.8%), potassium chloride (KCl, 99.5%), and Humic Acid (HA), were provided by Innochem Reagent Co., Ltd (Beijing, China). Sodium nitrate ($NaNO_3$, 99.0%) was provided by Furui (Beijing, China). The HA stock solution was prepared by dissolving HA powder in deionized water with a concentration expressed in the form of total organic carbon (TOC), which was measured through a TOC analyzer (TOC 5000A, Shimadzu, Japan).

2.2 Synthesis of Fe-based nanomaterials

Three types of Fe-based nanomaterials, nZVI, S-nZVI, and nFeS were prepared through modified borohydride-reduction approaches (He and Zhao, 2007; He et al., 2007; Tian et al., 2020). The photo and UV-Vis spectrum of three Fe-based materials were shown in Figs. S1 and S2. The detailed synthesis procedures are:

nZVI: In a typical preparation, $FeSO_4·7H_2O$ (0.0496 g)

was dissolved into 50 mL of deionized water in a flask, and a borohydride solution (10 mL, 1.35 g/L) was injected into the Fe solution within 3 min through an injection pump (Landa, Shanghai, China). The injection was performed under N_2 (⩾ 99%) purging with the flask shaken at 250 r/min (2.45 g) on a shaker. The nZVI was aged for another 15 min under vacuum before use.

S-nZVI: nZVI was prepared by the above method. Besides a borohydride solution (10 mL, 0.26 g/L) and a Fe solution (50 mL, 0.772 g/L), a Na_2S solution (10 mL, 1.67 g/L) was introduced into the flask to perform the sulfidation, and the formed particles were aged for 15 min. The mass ratio of Fe^0 to FeS is 1:1. Thus, the S/Fe ratio is 0.50.

nFeS: The Fe^{2+} solution (50 mL, 0.632 g/L) was purged with N_2 for 10 min to remove dissolved oxygen (DO). Then, Na_2S solution (10 mL, 2.73 g/L) was injected to the flask in 3 min. The mixture solution was then shaken at 250 r/min (2.45 g) for 15 min to ensure complete reaction until nFeS were formed. For nFeS, the S/Fe ratio is 0.57.

2.3 Batch experiments

Before use, the freshly synthesized Fe-based nanomaterials were washed with degassed deionized water for three times to remove residual salts. The suspension was mixed at 350 r/min (4.79 g) with a shaker. Then, batch tests were initiated by adding 10 mg of each nanomaterial into a 500 mL solution containing 10 mg/L Cd(II). Initial aqueous pH (pH_0) was adjusted to 4.0, 6.0, or 8.0 with NaOH (0.1 mol/L) and HCl (0.1 mol/L), with no attempt to maintain pH during experiments. The solution pH was measured by pH meter (Five Easy Plus, Mettler Toledo, Switzerland).

For all Cd(II) removal experiments, approximately 5 mL of suspension was sampled at given time intervals and filtered by a 0.22 μm membrane (Navigator, Tianjin, China). To ensure data quality, each experiment was performed in duplicate. Data were plotted as means of duplicates and the error bars (calculated as standard deviation) indicated data reproducibility. Cd(II) concentrations in all samples were quantified by the 884 Professional Volt-Ann electrode spectrometer with a detection limit of 0.1 μg/L (884 Professional VA, Metrohm, Switzerland). The ORP values were detected by an ORP meter (LE510, Mettler-Toledo, Switzerland). The concentrations of Fe were measured by UV (UV7, Mettler-Toledo, Switzerland) per an established method (Lee et al., 2014).

2.4 Characterization

The properties of nZVI, S-nZVI, and nFeS particle were analyzed using a set of crystallography, microscopy, and surface chemistry methods. The crystal structure was determined by powder x-ray diffraction (XRD) using a Brucker D8 Advance (Brucker, Germany) with Co $K\alpha$ radiation at a scan rate of 1.5°/min (2θ = 10°–90°). Rietveld refinements of XRD were computed by General Structure Analysis System (GSAS) software. The X-ray photoelectron spectroscopy (XPS) measurements were performed using a Thermo escalab 250Xi system (Thermo Fisher Scientific, USA). The zeta potential as well as hydromechanical diameter of samples were measured using a zeta potentiometer Dynamic Analyzer (Zetasier Nano ZS50, Thermo Fisher Scientific, USA). The Brunauer-Emmett-Teller surface area was determined by N_2 Physical adsorption/desorption assay on an ASAP 2460 (BET, Micromeritics, USA).

3 Results and discussion

3.1 Effect of nanomaterials doses on Cd(II) removal

Figure 1 shows the effect of the different nanomaterial doses (10, 20, and 50 mg/L) on the elimination of Cd(II) in contaminated solution, the amount of dissolution of Fe, and ORP values. Notably, the removal capacity of Cd by

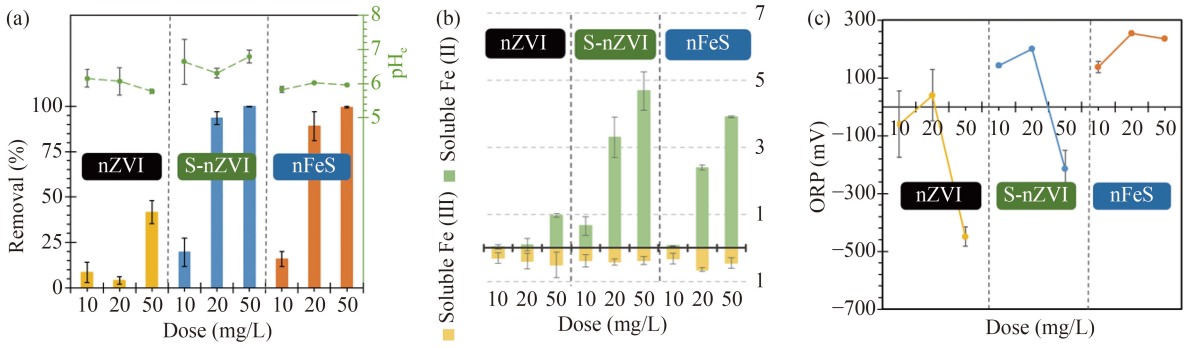

Fig. 1 Effect of doses of three Fe-based nanomaterials (10, 20, and 50 mg/L) on Cd(II) removal efficiency: (a) removal of aqueous Cd and final pH (pH_e) values; (b) Fe dissolution; and (c) redox potential (ORP) values (Experimental conditions: initial Cd(II) = 10 mg/L, t = 24 h, initial pH = 6.0. Data plotted as mean of duplicates and the error bars (calculated as standard deviation) indicate data reproducibility).

S-nZVI and nFeS were comparable to each other but significantly higher than nZVI (Fig. 1(a)). There was no significant improvement in the removal efficiency on Cd(II) with nZVI dose raised from 10 mg/L (8.40%) to 20 mg/L (4.10%). The Cd removal capacity increased further to 41.65% with the nZVI dose of 50 mg/L. However, when the S-nZVI dose increased from 10 to 20 mg/L, the Cd removal capacity improved from 19.60% to 93.50% (increase by a factor of ~4.8). The removal efficiency increased further to 99.95% at the dose of 50 mg/L. Similarly, the removal efficiencies for nFeS were 15.75% (at a dose of 10 mg/L), 89.12% (20 mg/L), and 99.52% (50 mg/L) under those same conditions. At the material dose of 20 mg/L, the S-nZVI and nFeS removal efficiency reached 93.50% and 89.12%, respectively, 22.8 and 21.7 times larger than that of nZVI (4.10%). After equilibrium, solution pH (pH_e) of nZVI group fluctuated between 5.7 and 6.2, was negatively correlated with increasing material dose, and reached a minimal pH at 50 mg/L (pH_e = 5.8). While the pH_e values of S-nZVI (pH_e ranged 6.3–6.8) and nFeS (5.8–6.0) fell into a narrower range.

Figure 1(b) shows the dissolved concentration of Fe, which indicates Fe dissolution since concentration was initially negligible. Apparently, the dissolution of total Fe was positively correlated with the material doses. Moreover, both total Fe and Fe(II) dissolution followed the concentration magnitude order S-nZVI > nFeS > nZVI. When the material dose was 20 mg/L, the total Fe dissolved from S-nZVI and nFeS respectively were 3.70 mg/L and 3.04 mg/L, and both were higher than nZVI (0.49 mg/L). Notably, the Fe(III) dissolution of nZVI (0.35 ± 0.15 mg/L), S-nZVI (0.39 ± 0.02 mg/L), and nFeS (0.48 ± 0.17 mg/L) were comparable under the three dose conditions, which may due to the limited solubility of Fe(III).

Figure 1(c) represents the ORP values at equilibrium. Based on these results, doses of 10 and 20 mg/L did not fully achieve a highly-reduced solution resulting in positive ORP values. A higher dose (50 mg/L) of nZVI and S-nZVI both developed a reducing condition with ORP values of −449.5 mV and −214.5 mV, respectively. However, at nFeS dose of 50 mg/L, the reaction was ultimately sustained as an oxidative condition (ORP = 236.5 mV).

Overall, the removal efficiency was significantly increased with elevated doses for three types of nanomaterials. Higher doses of materials provide more abundant reactive sites and reagents for Cd removal reactions until the maximum removal has been reached, and a similar and consistent trend was reported in previous studies. Boparai et al. found Cd removal increased from 22.5% to ~100% with a nZVI dose increased from 0.1 to 0.5 g/L (Boparai et al., 2013), and Liang et al. reported that when the S-nZVI dose increased from 0.2 to 0.4 g/L, the percent Cd removal increased from 7.6% to 62.0% (Liang et al., 2021a).

Interestingly, our results revealed that S-nZVI and nFeS had increased removal of Cd(II) compared to nZVI with same doses and conditions. The removal efficiency of S-nZVI and nFeS were nearly twice or more than that of nZVI (Fig. 1(a)). This discrepancy was mainly caused by their different Cd removal mechanisms, which were reported by previous studies but not compared systematically. Prior work suggests aqueous Cd(II) removal involves a rapid diffusion of Cd ions into nZVI particles and surface complexation between Cd(II) and iron hydroxides (Zhang et al., 2014; Liang et al., 2021b). While better Cd removal performances of S-nZVI and nFeS compared to nZVI have been mainly ascribed to the formation of iron sulfide precipitation. It is suggested that the key reaction mechanism between Cd(II) and S-nZVI is the replacement of Fe in FeS resulting in the formation of CdS (Hyun et al., 2021). Moreover, the sulfidation of nZVI can be inhibited by its aggregation. The hydrodynamic diameter of nZVI was 6727 nm, which was much greater than that of S-nZVI (5308 nm) and nFeS (2849 nm). The detailed discussion for the comparison on Cd(II) removal mechanisms by three Fe-nanomaterials can be found in Section 3.6.

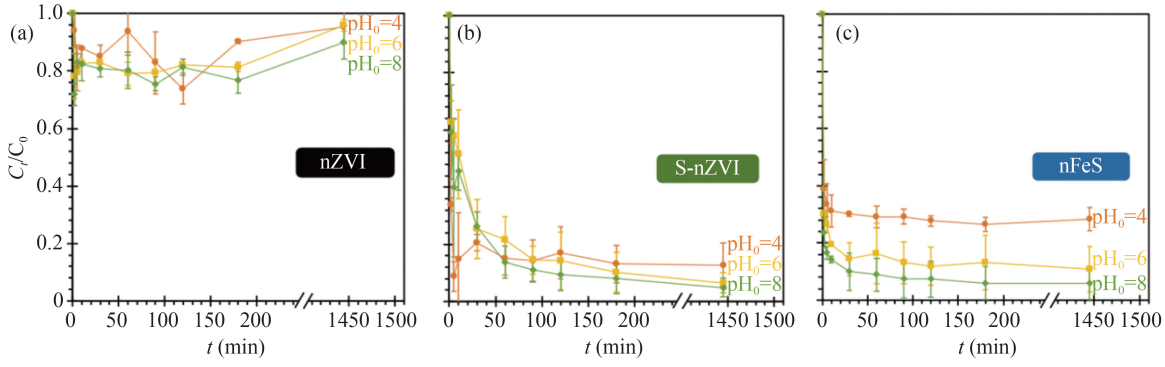

Fig. 2 Effect of pH on Cd(II) removal kinetics by three Fe-based nanomaterials, (a) nZVI, (b) S-nZVI, and (c) nFeS (Experimental conditions: initial Cd(II) = 10 mg/L, material dose = 20 mg/L).

3.2 Effect of pH on Cd(II) removal

As shown in Fig. 2, the Cd(II) removal by three nanomaterials varied greatly with variability of initial pH conditions. Similar to the trend reported in Fig. 1(a), the Cd(II) removal by three materials followed the order of S-nZVI > nFeS > nZVI. In addition, the removal efficiency increased at higher pH for all three materials. However, Cd removal by nZVI was the lowest of the three nanomaterials (Fig. 2(a)). nZVI gave a fast initial Cd(II) removal at first 30 min, yet, Cd(II) rebounded after 120 min for all three pH values, suggesting the dissolution of Cd. For S-nZVI and nFeS, the aqueous Cd concentrations drop at first rapidly within 30 min, and then concentrations stabilized with minor fluctuations. While S-nZVI gave the best removal performance (Fig. 2(b)). At 180 min, the removal capacity were higher than 85% for three cases, and no Cd(II) release was detected later. The removal efficiency of Cd by nFeS was lower than S-nZVI (Fig. 2(c)). For nFeS at 180 min, the removal capacities were 71.75% at pH 4, 89.12% at pH 6, and 94.08% at pH 8. At pH = 8, the removal efficiency of both S-nZVI and nFeS were almost identical.

To evaluate the kinetics of Cd(II) removal by Fe-based nanomaterials, pseudo-first-order (Eqs. (1) and (2)) and pseudo-second-order (Eqs. (3) and (4)) models were used and their expressions are (Du et al., 2016; Gong et al., 2017):

$$\frac{\mathrm{d}q_t}{\mathrm{d}t} = k_1(q_\mathrm{e} - q_t), \tag{1}$$

$$\text{Linearized form}: \ln(q_\mathrm{e} - q_t) = \ln q_\mathrm{e} - k_1 t, \tag{2}$$

$$\frac{\mathrm{d}q_t}{\mathrm{d}t} = k_2(q_\mathrm{e} - q_t)^2, \tag{3}$$

$$\text{Linearized form}: \frac{t}{q_t} = \frac{1}{k_2 q_\mathrm{e}^2} + \frac{1}{q_\mathrm{e}} t, \tag{4}$$

where q_t (mg/g) and q_e (mg/g) are the adsorption capacity of Cd(II) at time t (min) and equilibrium, respectively. Constants k_1 (1/min) and k_2 (g/(mg·min)) are the kinetic rate constants for the pseudo-first-order kinetic and pseudo-second-order kinetic models, respectively.

The model parameters were estimated through iterative calibration with the optimization objective of minimizing the deviations between the model and the observed data to provide the best fit between the model result and observations. The fitting parameters for both models and three materials were tabulated in Table S1 in Supporting Information (SI), and the comparisons of modeled results and observed data were plotted in Fig. S3. Generally, the pseudo-second-order model provided a closer match to the observations than the pseudo-first-order model with a much larger R^2, which agreed with the findings of other researchers (Du et al., 2016; Gong et al., 2017). This indicated that chemical adsorption is the rate-limiting step in the displacement reaction (Gong et al., 2017; Liang et al., 2020). Moreover, the pseudo-second-order model did not give a reasonable match to describe the observed data for nZVI due to the rebound of Cd(II) after 120 min (Fig. S3). Thus, only the data for the initial stage with fast removal was used to give a fair comparison. Furthermore, the reaction rate constant at initial stage of nZVI (k_2 = 0.0062 g/(mg·min)) was larger than the sulfidated nZVI (k_2 = 0.0004 g/(mg·min) of S-nZVI, k_2 = 0.0024 g/(mg·min) of nFeS). This may be due to the formation of CdS inhibiting the contact of Cd with the active site within the particle, resulting in a lower k_2 (Liang et al., 2020; 2021a). Thus, a larger rate constant and fast reaction rate did not lead to a higher removal capacity for Fe-based nanomaterials.

Figure 3(a) illustrates the pH changes for each of the three nanomaterials during reactions. For all the materials, at initial pH ($\mathrm{pH_0}$) of 4, the final pH ($\mathrm{pH_e}$) values were increased. While for $\mathrm{pH_0}$ of 6, the solution pH were well buffered and remained stable for all three

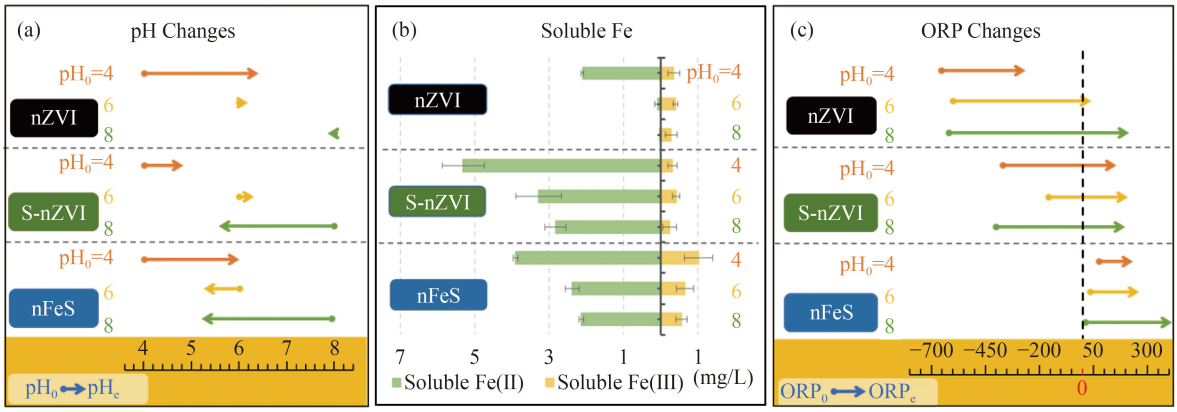

Fig. 3 Effect of pH on Cd(II) removal by three Fe-based nanomaterials. (a) changes of pH after the reaction equilibrium (arrowed from $\mathrm{pH_0}$ to $\mathrm{pH_e}$); (b) Fe dissolution; and (c) ORP values (Experimental conditions: initial Cd(II) = 10 mg/L, material dose = 20 mg/L, t = 24 h, initial $\mathrm{pH_0}$ = 4, 6, or 8).

materials. However, at pH_0 = 8, the final pH values for nZVI, S-nZVI, and nFeS were 8.0, 5.6, and 5.3, respectively. Overall, it seems that nFeS can buffer the solution pH into a narrow range (~5 to 6). Figure 3(b) shows the dissolution of both Fe(II) and Fe(III). Apparently, higher total Fe and Fe(II) releases were observed at more acidic solutions for all three materials. Fe(III) release concentrations at pH_0 of 4 and 6 were comparable, but was generally lower at pH_0 of 8. Again, S-nZVI and nFeS released more Fe than nZVI, which was consistent with the trend observed in Fig. 1(b). ORP changes were plotted in Fig. 3(c). It was clear that the initial ORP (ORP_0) value of nZVI and S-nZVI solutions were negative, and when the reaction reached equilibrium, the solution of all three materials exhibited an oxidative potential (positive ORP_e values), except for nZVI with pH_0 of 4.

The species of cadmium in aqueous solution are closely associated with pH (Fig. S4). Cd(II) is dominant at pH < 9. As pH increases, cadmium hydroxides become more abundant. Solid $Cd(OH)_2$ forms at pH ~8.7 and becomes predominant at pH > 9. Accordingly, Cd(II) is more favored to precipitate at basic pH values. At pH = 6–8, the main speciation of cadmium are Cd^{2+} or $Cd(OH)^+$, which has more absorption onto the negatively charged nZVI, and Cd also precipitates at the higher pH range. This trend was also reported by Reed and Matsumoto (1993).

Moreover, variation of aqueous pH influences Fe-nanomaterial properties. For nZVI, firstly, its pH_{ZPC} (the point of zero charge at which the net surface charge of particle is zero) is 6.9 (Fig. S5), and the surface of the nanomaterial exhibited a negative charge at pH values above 6.9. Thus, positively charged Cd(II) has a larger electrostatic attraction to nZVI at higher pH. Secondly, aging reactions and Fe^0 corrosion would be more favorable to occur in acidic solutions (Eqs. (5) and (6)) (Qiao et al., 2018). Therefore, increased Fe concentrations and release were observed for nZVI at pH = 4 (Fig. 3(b)). Aqueous Cd had an adsorptive affinity to iron corrosion products, which acted as contaminant scavengers (Touomo-Wouafo et al., 2018; Huang et al., 2020). Corrosion or dissolution of Fe^0 leads to release of Cd within acidic solutions. Thirdly, the metal oxide coatings on nZVI surfaces can stabilize the aqueous solution following Eqs. (7)–(9) (Zhang et al., 2016a). These buffering reactions can further alter the surface charge of nanomaterials and solution pH. Interestingly, the final pH values for nZVI fell into the narrow range of 6–8 (Fig. 3), which provides evidence for pH buffering. Fourth, Cd(II) removal reaction per surface complexation would produce H^+, and this reaction is more prevalent within basic solutions (discussed in Section 3.6).

$$Fe^0 + 2H_2O \rightarrow Fe(OH)_2 + H_2 \quad (5)$$

$$Fe^0 + 2H^+ \rightarrow Fe^{2+} + H_2 \quad (6)$$

$$\equiv Fe^{2+} + 2H_2O \leftrightarrows \equiv Fe(OH)_2 + 2H^+ \quad (7)$$

$$\equiv FeO_2H_3^+ + OH^- \leftrightarrows \equiv Fe(OH)_2 + H_2O \quad (8)$$

$$\equiv Fe(OH)_2 + 2OH^- \leftrightarrows \equiv FeO_2^- + 2H_2O \quad (9)$$

The removal capacity was significantly increased for two sulfidated Fe-based nanomaterials compared to nZVI. Firstly, pHzpc of S-nZVI (pH_{ZPC} = 6.7) and nFeS (pH_{ZPC} = 5.4) were lower than that of nZVI (pH_{ZPC} = 6.9) (Fig. S5). The surface charge of nFeS had a negative charge over a larger pH range (Zhang et al., 2014; Sun et al., 2017; Lv et al., 2018). Secondly, the corrosion of FeS was also highly pH-dependent as discussed in Section 3.6, and corrosion was more favored to occur under acidic pH. Thirdly, at higher pH, Cd readily reacted with S^{2-} to form CdS (Fig. S6), and iron hydrate produced by Fe hydrolysis in solution to form a solid precipitate, which facilitates acceleration of the Cd removal (Hyun et al., 2021).

3.3 Effect of co-existing ions on Cd(II) removal

Figure 4 presents the effect of co-existing ions (Na^+,

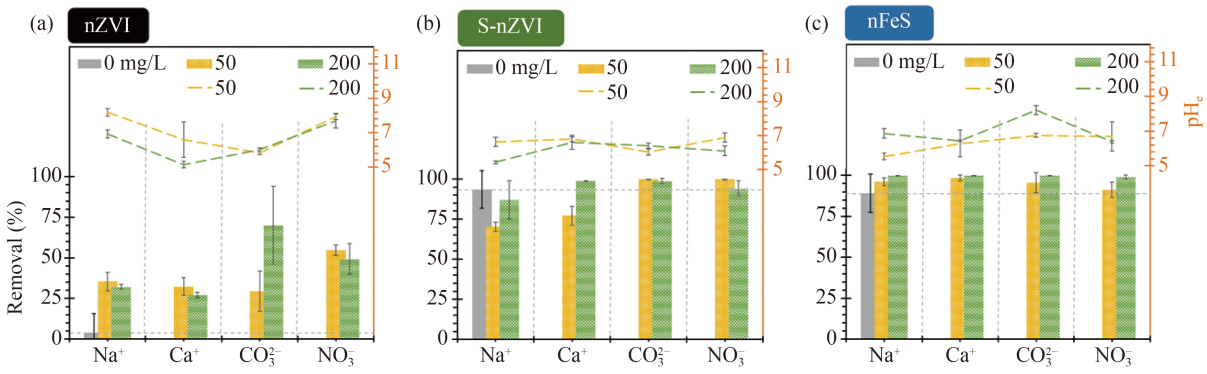

Fig. 4 Effect of co-existing ions on Cd(II) removal by three Fe-based nanomaterials: (a) nZVI, (b) S-nZVI, (c) nFeS (Experimental conditions: initial Cd(II) = 10 mg/L, initial pH = 6.0, material dose = 20 mg/L, t = 24 h, the introduced ions = 0, 50, or 200 mg/L).

Ca^{2+}, CO_3^{2-}, and NO_3^-) on Cd(II) removal by each of the three Fe-based nanomaterials. The added ions influenced the behavior of nanomaterials differently. For nZVI, the presence of co-existing ions leaded to higher Cd(II) removal, and increased or comparable removal efficiency was observed with higher ionic strength. Notably, the Cd(II) removal increased from 4.10% (without additional ions) to 29.45% with 50 mg/L of CO_3^{2-} and to 70.00% with 200 mg/L of CO_3^{2-}. While for S-nZVI, the introduction of Na^+ suppressed Cd removal. The Cd removal was inhibited by Ca^{2+} from 93.50% (without additional ions) to 77.25% (Ca^{2+} of 50 mg/L), but increased to 98.98% upon increasing the dose of Ca^{2+} to 200 mg/L. The presence of CO_3^{2-} and NO_3^- slightly increased Cd removal. For nFeS, increasing the dose of coexisting ions resulted in enhanced Cd removal in all cases. The introduced ions influence the final pH of nZVI more greatly than that of S-nZVI and nFeS (Fig. 4). Figure S7 shows the dissolution of Fe with the presence of co-existing ions. We can conclude that ion strength had no obvious effect on the Fe(III) dissolution. It is noteworthy that the presence of CO_3^{2-} has a great inhibition on Fe(II) dissolution for both sulfide materials. As shown in Fig. S8, the final ORP values again follow the order of nZVI < S-nZVI < nFeS.

Generally, cations (Na^+ and Ca^{2+}) and anion like NO_3^- do not impact Cd(II). While theoretical calculation revealed that with the presence of CO_3^{2-}, Cd(II) can form $CdCO_3$ easily even at lower pH or $Cd(OH)_2$ at higher pH (Fig. S9), resulting in a greatly enhanced precipitation. Furthermore, the co-existing ions can also influence the Fe-nanomaterial behavior. Cations (Na^+ and Ca^{2+}) significantly enhanced Cd removal capacity (Fig. 4). This may be due to the salting-out effect on Cd solubility by elevated ionic strength with these two cations. Previous studies also reported that Fe-based nanomaterials solution exhibited increased corrosion in solutions containing Na^+ and Ca^{2+} than in deionized water (Turcio-Ortega et al., 2012). In general, greater corrosion current results from higher degrees of iron oxidation at the surface, which implies greater reductive transformation or complexation of metal ions by Fe materials (Kim et al., 2013; Sun et al., 2016). The added CO_3^{2-} can also cause a portion of Fe to precipitate as $FeCO_3$ per Eq. (10) (also as shown in Fig. S9), facilitating the removal of Cd (Fig. 4) while also inhibiting the dissolution of Fe from the nanomaterials (Fig. S7). The addition of NO_3^- can react with nZVI per Eq. (11) (Liang et al., 2020).

$$Fe^{2+}CO_3^{2-} \rightarrow FeCO_3 \quad (10)$$

$$NO_3^- + 3H_2O + 3Fe^0 \rightarrow NH_4^+ + 2OH^- + Fe_3O_4 \quad (11)$$

According to Eq. (11), OH^- can be produced and an increase of final pH was also observed in our study (Fig. 4(a)), which was also consistent with the conclusion of Su et al. (2014). In summary, the added ions can enhance a higher corrosion current in solutions and influence the formation of $Cd(OH)_2$ and $CdCO_3$ to improve the removal efficiency of Cd(II).

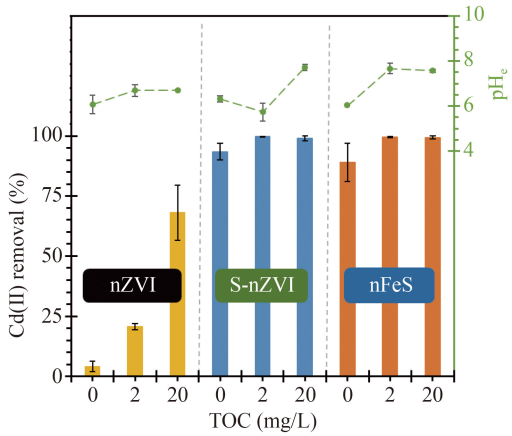

Fig. 5 Effect of HA (expressed as TOC) concentration on Cd(II) removal by three Fe-based nanomaterials (Experimental conditions: initial Cd(II) = 10 mg/L, initial pH = 6.0, material dose = 20 mg/L, t = 24 h).

3.4 Effect of HA on Cd(II) removal

Figure 5 shows the removal of Cd(II) by three Fe-based nanomaterials with the presence of different concentrations of humic acid (as TOC = 2 or 20 mg/L). When the concentration of HA increased, the removal capacity of Cd(II) in three cases all increased. This trend was more evident in the case of nZVI. When the HA concentrations increased to 2 and 20 mg/L, the Cd(II) removal increased from 4.10% (no HA) up to 20.65% (5-fold increase) and 68.10% (17-fold increase), respectively. In the cases of S-nZVI and nFeS, the presence of HA improved the Cd removal even more. For three Fe-based nanomaterials, higher concentration of HA (as 20 mg/L of TOC) also lead to a pH increase. However, the ORP values decreased at higher TOC concentrations (Fig. S10). As shown in Fig. S11, the dissolution of Fe had a significant increase for nZVI as TOC increased from 0 mg/L to 20 mg/L. While the trend was different for S-nZVI and nFeS.

The reason for the increased removal capacity with the presence of TOC can be addressed that the HAs have abundant carboxylic acid and phenolic acid groups, which exhibit considerable affinity for divalent metal ions, and can easily complex with Fe^{2+} and Cd^{2+} (Brigante et al., 2009). Tian et al has also reported that adsorbed HA may facilitate adsorption of Cd^{2+} through surface complexation (Tian et al., 2020). Organic matter can also act as a catalyst or provided an electronic shuttle channel to promote removal of pollutants, as suggested by Neumann et al. (2011). Previous study also reported that in ternary systems (Cd - HA - metallic oxide), the presence of HA leads to an increase in Cd(II) adsorption owing to enhanced surface complexation (Davis and Bhatnagar, 1995).

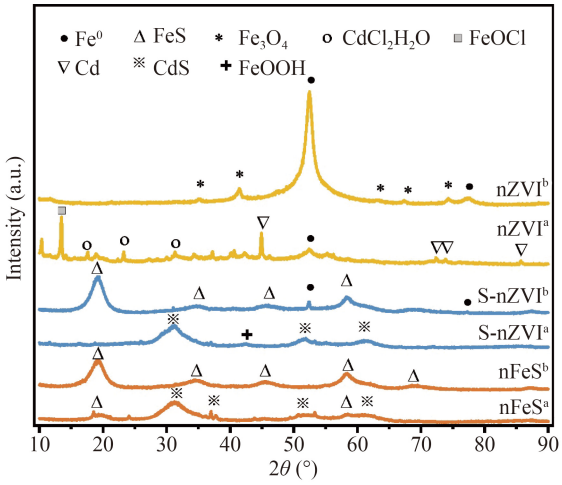

Fig. 6 XRD analysis results for Fe-nanomaterials before (labelled with superscript b) and after (labelled with superscript a) reaction with Cd.

3.5 Characterizations on materials before and after reaction

XRD studies: XRD patterns of three freshly prepared and reacted materials are shown in Fig. 6. For fresh nZVI (as nZVI^b in Fig. 6), the peak at 2θ of 52° signals the presence of Fe^0 (PDF#89-7194). Additionally, there were small peaks at about 35.5°, 42°, and 75° of 2θ assigned to Fe_3O_4 (PDF#88-0866), which was formed after preparation and covered the Fe^0 core as a shell with little quantities (7.2% wt. as computed per Rietveld refinement) compared to Fe^0 (Abdel Salam et al., 2021). After the reaction with Cd (as nZVI^a in Fig. 6), the characteristic peak of Fe^0 decreased dramatically, suggesting the consumption of nZVI and partial oxidation of iron. New peak were detected at 2θ of 13.5° (PDF#76-2300) suggested the main oxidation product was Fe(III), which was consistent with the XPS results. The existence of little quantities (8.9% as computed per Rietveld refinement) Cd^0 after reaction suggested that part of Cd(II) was reduced, which is consistent with the study of Su et al. (2014). However, reduction of Cd(II) to Cd^0 by nZVI was not observed in another study (Zhang et al., 2014). This discrepancy may be caused by the difference of nZVI dose or aqueous matrix. For fresh S-nZVI (as S-nZVI^b in Fig. 6), the peaks at 2θ of 52.5°, and 2θ of about 20°, 35°, 45.5° and 58° signal the presence of Fe^0 and mackinawite (FeS, PDF#89-2738), respectively. The presence of abundant (96.8%) FeS conformed to the crystallinity of S-nZVI particles, which was consistent with the study of He et al. (2012). However, Fe^0 and Fe_3O_4 were the predominant components for S-nZVI in the study of Liang et al, probably because the FeS existed in an amorphous form (Liang et al., 2020). Liang also found that part of the sulfide was oxidized to S^0 after S-nZVI reacted with metals (Liang et al., 2021a). After the reaction (as S-nZVI^a in Fig. 6), the XRD peaks at 2θ of 31°, 51.8°, and 61.8° confirmed the formation of CdS (PDF#80-0019), and the iron oxide was FeO(OH) (2θ =16.5°, PDF#70-0714), which was consistent with previous results (Liang et al., 2020). For fresh sample of nFeS (nFeS^b), the peaks at 2θ of about 20°, 35°, 45.5°, 58°, and 69° were attributed to FeS (PDF#89-2738), and no iron oxides were identified. These results agreed with the findings of Tian et al. (2020). After reacting with Cd (nFeS^a), peaks for CdS was also identified.

XPS studies: To further study the Cd removal mechanisms by these three materials, XPS was used to reveal the element composition and distribution on sample surface, and the changes of the chemical valence states before and after the reactions were also evaluated. As shown in broad survey of three fresh and reacted materials (Fig. S12), peaks represented for Cd 3d (binding energy of ~405 eV and ~412 eV) appeared after reaction. The XPS spectra of Cd is given in Fig. S13, which also indicated two intense peaks for Cd $3d_{3/2}$ and Cd $3d_{5/2}$ (Wu et al., 2006; Lv et al., 2018). And the speciation of Cd(0) in XPS were found in Hou's study (Hou et al., 2022). Thus, these results confirmed that Cd(II) was immobilized on the surface of materials (Zhang et al., 2014).

Detailed XPS spectra for Fe 2p (Fig. 7), S 2p (Fig. 8) and O 1s (Fig. S14) were systematically compared and peak splitting parameters can be found in Tables S2–S5. For fresh nZVI (Fig. 7(a)), a small peak at ~707 eV suggested the existence of zero-valent iron (Boparai et al., 2013). The peak at ~711 eV was attributed to Fe $2p_{3/2}$ for FeO (Lv et al., 2018). The presence of photoelectron peaks at ~713 eV for Fe $2p_{3/2}$, and ~725 eV for Fe $2p_{1/2}$ suggested the existence of Fe(III) on the fresh nZVI surface (Xu et al., 2016), which was consistent with the XRD results (Fig. 6). The peak at ~719 eV was considered as the satellite peak of Fe $2p_{3/2}$ (Yamashita and Hayes, 2008). The above-mentioned phenomenon indicated the formation of a layer of iron oxides. The coexistence of a large fraction of iron oxides and a relatively small amount of Fe^0 confirmed the core-shell structure of nZVI (Wu et al., 2006; Lv et al., 2018). After reaction, the peak of Fe^0 disappeared implying the oxidation of Fe^0. There was no obvious change on proportions of Fe(II) and Fe(III). O 1s survey scans (Fig. S14(a)) were conducted to study the oxygen species on the surface. Before reaction, the photoelectron peaks decomposed into two peaks at ~530 eV and 531.5 eV, corresponding to the binding energies of O^{2-} and -OH, respectively (Zhang et al., 2014). The O^{2-} peak contributed ~17% of the total O 1s peak area. After reaction, only the peak of -OH was remained.

Figure 7(b) shows that for pristine S-nZVI, the chemical valence states were similar to those of nZVI, but with different proportions. For Fe(II) with the peak of ~711 eV, it was likely to be Fe(II)-O/Fe(II)-S (Lv et al., 2018). After reaction, the peak of Fe^0 disappeared due to oxidative

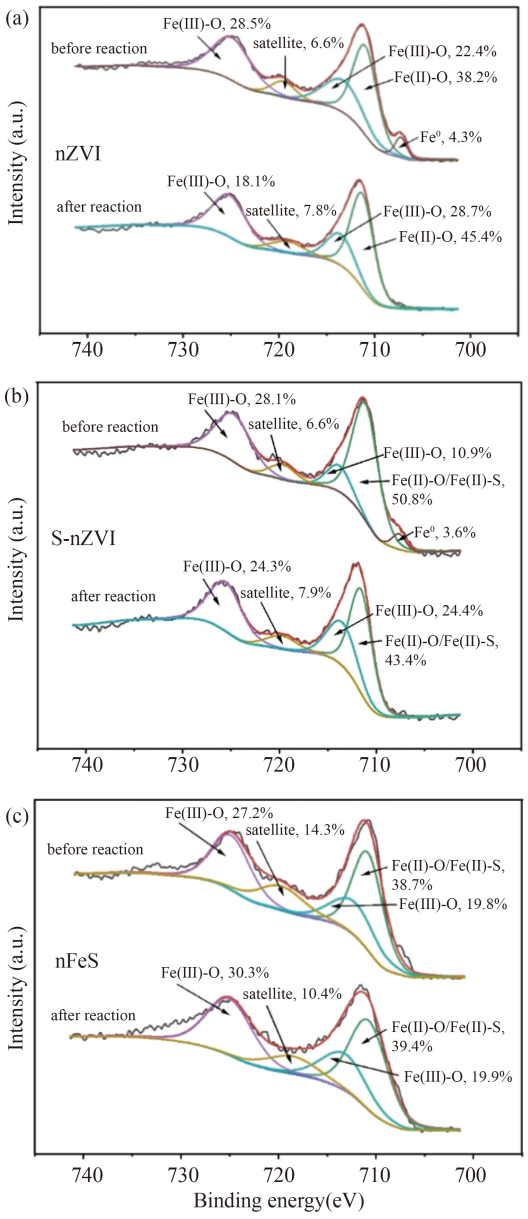

Fig. 7 Spectra results for Fe 2p for (a) nZVI, (b) S-nZVI, and (c) nFeS.

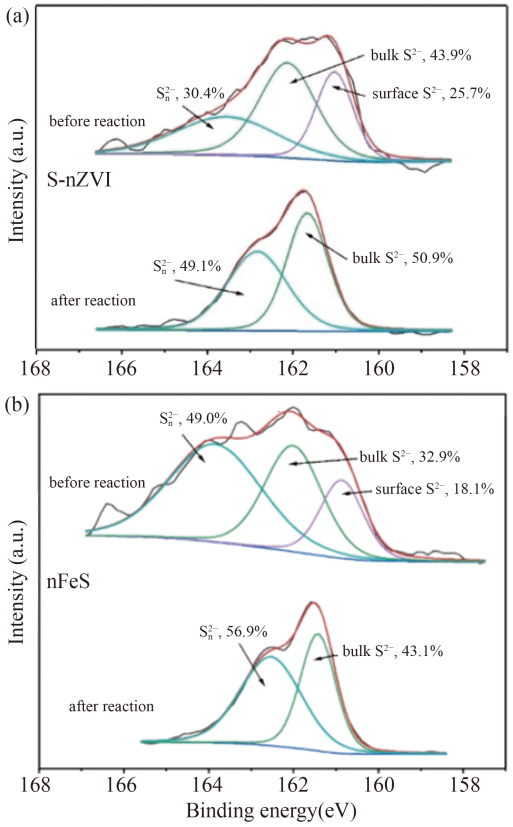

Fig. 8 XPS spectra results for S 2p for (a) S-nZVI and (b) nFeS.

transformation. The XPS spectrum of S 2p (Fig. 8(a)) had three peaks at around 161 eV, 162 eV, and 163.5eV for S-nZVI before reaction, which were considered as the peaks of surface S^{2-}, bulk S^{2-}, and S_n^{2-}, respectively. After reaction, two peaks remained around 161.7 eV and 162.8 eV for bulk S^{2-} and S_n^{2-}, respectively (Dong et al., 2018; Liang et al., 2021b). For the O 1s spectrum of fresh material (Fig. S14(b)), the peak of -OH (binding energy of ~530 eV) and O^{2-} (531.7 eV) accounted for 84.6% and 15.4%, respectively (Rajajayavel and Ghoshal, 2015). Again, the O^{2-} peak disappeared after reaction.

Figure 7(c) shows for nFeS before reaction, the Fe 2p peaks at ~711 eV and ~712 eV corresponded to Fe $2p_{3/2}$ for Fe(II) and Fe(III), respectively; and the peaks at ~725 eV was assigned to Fe $2p_{1/2}$ of Fe(III). The satellite peak also existed at ~719 eV (Du et al., 2016; Sun et al., 2017). After reaction, there was no obvious change in the proportions of all the peaks. For the fresh sample (Fig. 8(b)), the peaks of surface S^{2-}, bulk S^{2-}, and S_n^{2-} appeared at 160.7 eV, 161.6 eV, and 163.1 eV, respectively. After reaction, only bulk S^{2-} and S_n^{2-} remained, at 161.4 eV and 162.5 eV (Jeong et al., 2010). In addition, Fig. S14(c) showed that after reaction, the peaks of O^{2-} decayed.

3.6 Comparison on Cd(II) removal mechanisms for three Fe-nanomaterials

Our results demonstrated that S-nZVI and nFeS achieved better Cd(II) removal than nZVI under the identical conditions. This discrepancy was mainly due to their different Cd removal mechanisms and here, we provide a systematical comparison.

nZVI: For nZVI, different removal mechanisms were involved. Previous studies reported that Cd(II) removal appeared to involve a rapid diffusion of Cd(II) into nZVI particles and surface complexation of Cd(II) with iron hydroxides per (≡ denotes the surface) (Zhang et al., 2014; Liang et al., 2021b):

$$\equiv FeO^- + Cd^{2+} \rightarrow \equiv FeOCd^+ \quad (12)$$

$$\equiv FeOH + Cd^{2+} + H_2O \rightarrow \equiv FeOCdOH + 2H^+ \quad (13)$$

The results and opinions on whether Cd can be reduced by nZVI were mixed. The theoretical standard potential of Fe^0 is quite close with Cd (Eqs. (14) and (15)) (Boparai et al., 2013; Zhang et al., 2014; Huang et al., 2020). Thus, a direct reduction seems unlikely as suggested by some researchers and no reduced Cd was detected (Zhang et al., 2014).

$$Fe^0 \rightarrow Fe^{2+} + 2e^-,\ E^0 = -0.41\ V \quad (14)$$

$$Cd^0 \rightarrow Cd^{2+} + 2e^-,\ E^0 = -0.40\ V \quad (15)$$

However, the formation of elemental Cd was also reported and detected in some other studies (Su et al., 2014; Hou et al., 2022). Interestingly, our XRD results demonstrated the formation of Cd^0, while that was not reflected by the XPS spectra. This discrepancy could be mainly due to the fact that general XPS can only detect the surface components (Sun et al., 2016). Thereby, we speculated that the formed Cd^0 was encapsulated into the nZVI particles. The mechanisms involving sorption, followed by diffusion, and then encapsulation of target metal ions by nZVI, was proven by high-sensitivity X-ray energy-dispersive spectroscopy-scanning transmission electron microscopy (XEDS-STEM) previously (Ling et al., 2017). Similarly, in our study, the encapsulated Cd was detected by XRD, but not XPS. In addition, the spent nZVI particles became denser than the fresh ones (Ling et al., 2017), and a similar trend was observed in our work that the average hydrodynamic diameter of nZVI decreased from 6727 nm to 1158 nm after reaction. Thus, reduction of Cd(II) by nZVI was also an important role in Cd removal per:

$$Fe^0_{(s)} + Cd^{2+} \rightarrow Fe^{2+} + Cd^0_{(s)} \quad (16)$$

$$Cd^{2+} + 2Fe(OH)_{2(s)} + 2H_2O \rightarrow Cd^0_{(s)} + 2Fe(OH)_{3(s)} + 2H^+ \quad (17)$$

In summary, Cd(II) removal by nZVI involved coprecipitation, surface complexation, and reduction as shown in Fig. 9(a).

S-nZVI and nFeS: Sulfidation can modify nZVI for heavy metal removal in serval aspects: 1) the aggregation of nZVI particles can be efficiently prevented by sulfidation (Zhang et al., 2016b; Gong et al., 2017). The presence of van der Waal force, intrinsic magnetic interactions, and high surface energy can facilitate the aggregate of nZVI particles resulting in limited mobility (Phenrat et al., 2007; Min et al., 2008; Zhao et al., 2016). However, the sulfidation can produce iron sulfide coatings on the Fe^0 surface, effectively preventing the aggregation of particles; 2) For S-nZVI, the presence of delocalized electrons in the layers of iron sulfides can improve electron transfer capacity and electron transfer rate than the unmodified nZVI (Li et al., 2017); and 3) The sulfidation has been shown to enhance the immobilization of heavy metals as sulfides, which are more favored to precipitate and resistant to reoxidation (Fan et al., 2017).

There were also various Cd removal mechanisms associated with these two iron sulfide nanomaterials. Our results verified that the component of FeS in nanomaterials greatly enhanced the overall Cd(II) removal. The overall dominant reaction is the replacement of Fe in FeS in the particle and the formation of CdS as (Hyun et al., 2021):

$$FeS + Cd^{2+} \rightarrow CdS + Fe^{2+} \quad (18)$$

Some other side reactions include: Cd(II) precipitation with the corrosion products of FeS (Eqs. (19) and (20)) and a series of surface complexation reactions (Eqs. (21)–(24)):

$$FeS_{(s)} + H^+ \rightarrow Fe^{2+} + HS^- \quad (19)$$

$$Cd^{2+} + HS^- \rightarrow CdS + H^+ \quad (20)$$

$$\equiv S^- + Fe^{2+} \rightarrow \equiv SFe^+ \quad (21)$$

$$Cd^{2+} + FeS + 2H_2O \rightarrow CdS + 2Fe(OH)_{2(s)} + 2H^+ \quad (22)$$

$$\equiv S^- + Cd^{2+} \rightarrow \equiv SCd^+ \quad (23)$$

$$\equiv OH + Cd^{2+} \rightarrow \equiv OCd^+ + H^+ \quad (24)$$

In summary, Cd(II) removal by S-nZVI and nFeS involved replacement, coprecipitation, and surface

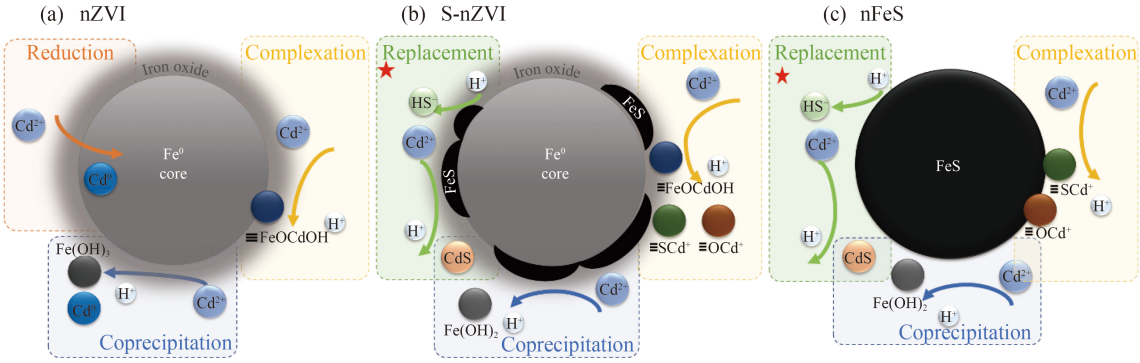

Fig. 9 Illustrations for the mechanism comparison schemes of (a) nZVI, (b) S-nZVI, and (c) nFeS.

complexation (Figs. 9(b) and 9(c)), and among which, the replacement reaction was the predominant. The difference between S-nZVI and nFeS was that, for S-nZVI, Eqs. (12) and (13) reaction could also occur as side reaction owing to the existence of small fraction of non-sulfide nZVI (Fig. 9(b)). Yet, the replacement reaction was so overwhelming that the other side reactions were negligible. Further discussion can be found in Section 3.7.

Key parameters (i.e., Cd removal (%), Cd(II) removal rate constants (k_2), final pH, removal capacity (mg/g), final ORP, and total Fe release) were plotted in a Radar chart (Fig. 10), which provides a comparison summary for these three nanomaterials. Clearly, Cd(II) removal by S-nZVI had advantages in most of aspects, with the highest Cd removal, a neutral final pH (6.31), the highest removal capacity (467.5 mg/g), which was significantly higher than those of other Fe-based materials under comparable conditions (Table S6), and moderate final ORP (200.5 mV). It is noteworthy that both S-nZVI and nFeS yielded a high Fe dissolution compared to nZVI. While for nFeS, most of the parameters were comparable with slightly lower Cd removal performance compared to S-nZVI, and nZVI had generally lower values for most parameters. However, the primary advantage of nZVI was its fast initial removal rate (k_2 of 0.0062 g/(mg·min)), which was much larger than S-nZVI and nFeS. Moreover, nZVI gave the lowest removal capacity, final pH of 6.07, the lowest final ORP (40.0 mV), and the lowest Fe dissolution (0.49 mg/L).

3.7 Relationship between Cd(II) removal and Fe(II) dissolution

Figure S15 gave the kinetics of Fe(II) dissolution for three nanomaterials. To investigate the relationship

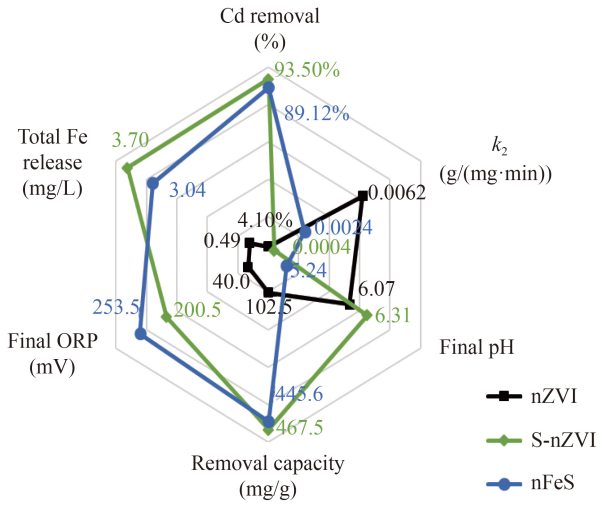

Fig. 10 Comprehensive comparison of the performance of Cd removal by nZVI, S-nZVI, and nFeS (Experimental conditions: initial Cd(II) = 10 mg/L, initial pH = 6.0, material dose = 20 mg/L, t = 24 h).

between Fe(II) release and Cd(II) removal, the removed Cd(II) (calculated as $C_0 - C_e$ of Cd(II)) as a function of released Fe(II) at the same time intervals were plotted in Fig. 11(a). A positive and linear relationship ($R^2 > 0.8$) for S-nZVI and nFeS were observed, except for the case of pH 6 for nFeS. This strongly positive correlation indicated that the dominant reaction mechanism for nFeS and S-nZVI was the replacement of Fe in FeS in the particle with the formation of CdS (Eq. (18)). Further, the stoichiometric ratio of Cd(II) to Fe(II) in the replacement reaction was 2 (calculated based on mass, and as shown by the dotted line in Fig. 11(a)), and slopes of the linear fittings were > 2 at pH 6 and 8, suggesting less Fe(II) dissolved than expected. A possible side reaction was proposed that dissolved Fe(II) may react to form a surface complex with the surface sulfide (Eq. (21)) (Hyun et al., 2021). The Fe(II) ions absorbed in the surface structure improved surface oxidation layer conductivity, and decreased the electron transfer barrier of the corrosion coating, leading to an enhanced electrons transfer (Mielczarski et al., 2005). Meanwhile, the disappearance of surface S^{2-} after reaction in the XPS surveys for S-nZVI and nFeS also supported this point. While the slopes were lower than 2 at pH 4 for both sulfide materials, denoting that dissolved Fe(II) was contributed by replacement reaction (Eq. (18)) and material decay reaction (Eqs. (5) and (6) for ZVI, and Eq. (19) for FeS). For nFeS at pH 6, the removed Cd(II) was not proportional to the dissolved Fe(II) concentration, which may be due to the fact that a fast release of Fe(II) was observed for the initial stage. For nZVI, the regression did not produce substantial correlations, and the R^2 values were smaller than 0.5 at various pH conditions. This again confirmed that Fe(II) dissolution was involved in more than one reaction mechanisms for nZVI. The dissolved Fe(II) may come from the Fe^0 corrosion in aqueous solution (Eqs. (5) and (6)) and a minor mechanism of Cd(II) reduction (Eqs. (16) and (17)).

Figure 11(b) presents correlations between the dissolved Fe(II) and the removed Cd(II) at the reaction equilibrium (24 h). Again, strong correlations were observed for S-nZVI and nFeS, while nZVI exhibited a very poor relationship. With the pH increased from 4 to 8 (Fig. 11(b)), the negative slopes of nFeS (−1.22) and S-nZVI (−0.31) indicated that the removed Cd(II) increased and the dissolved Fe(II) tended to be suppressed. Also, Fe(II) dissolution from nFeS posed a larger influence on removed Cd(II) than S-nZVI. In addition, there was also a strong, positive, and linear relationship between dissolved Fe(II) and removed Cd(II) at different Fe-based materials doses (Fig. 11(c)). Interestingly, for both sulfide materials, similar slopes in the linear correlation were observed, indicating that the variation of dosage posed negligible influence on the removal mechanism.

Based on pseudo-first-order and pseudo-second-order removal kinetic models, we propose a reaction-product

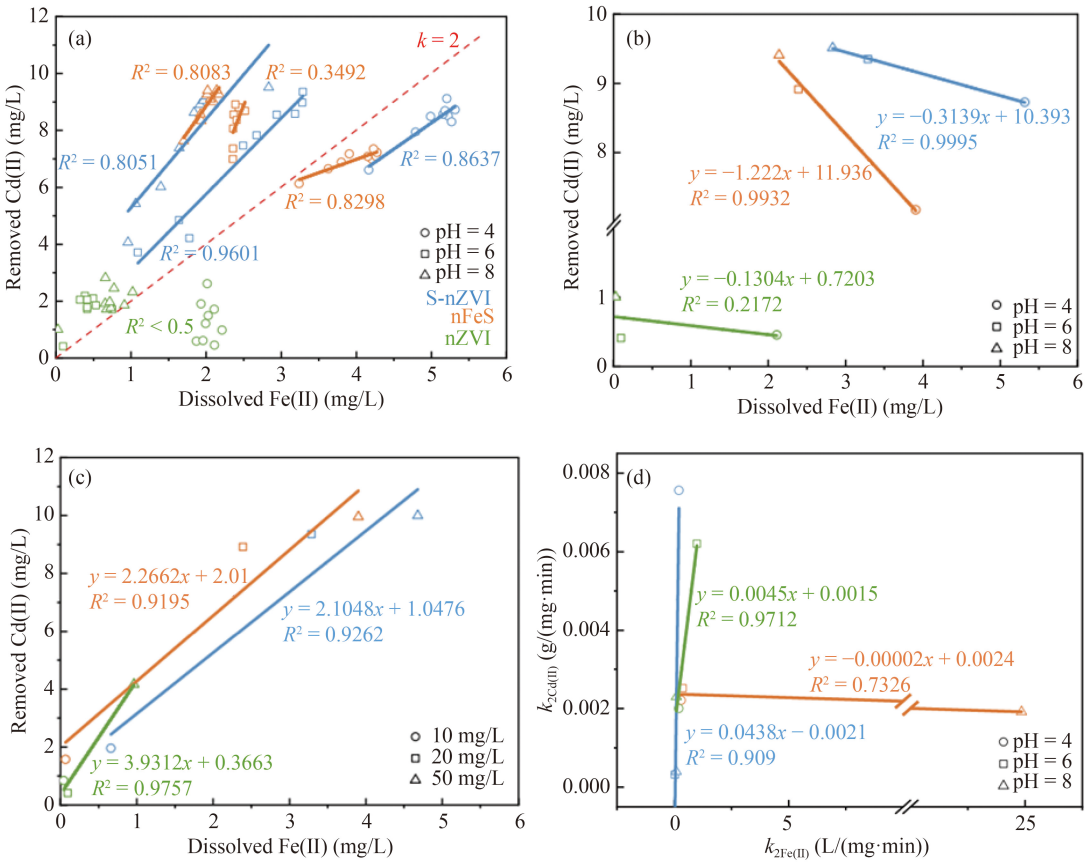

Fig. 11 Correlation between dissolved Fe(II) and (a) the removed Cd(II) at designed time intervals within 24 h; (b) the removed Cd(II) at various pH at 24 h, (c) the removed Cd(II) with different materials dosage at 24 h; and (d) the pseudo-second-order rate constants for Fe(II) dissolution and Cd(II) removal within 24 h at different pH values.

generation kinetic model for Fe(II) dissolution as:

$$\frac{dc_{tFe}}{dt} = k_{1Fe(II)}(c_{eFe} - c_{tFe}), \quad (25)$$

$$\text{Linearized form}: \ln(c_{eFe} - c_{tFe}) = \ln c_{eFe} - k_{1Fe(II)}t, \quad (26)$$

$$\frac{dc_{tFe}}{dt} = k_{2Fe(II)}(c_{eFe} - c_{tFe})^2, \quad (27)$$

$$\text{Linearized form}: \frac{t}{c_{tFe}} = \frac{1}{k_{2Fe(II)}c_{eFe}^2} + \frac{1}{c_{eFe}}t. \quad (28)$$

As an alternative to Cd(II) removal-decay kinetics, the released Fe(II) was assumed as a target reactant (i.e., as dominant or rate-limiting step) (Gong et al., 2017; Liang et al., 2020). Thus, theoretically, Fe(II) dissolution was considered as a reversed process of Fe(II) removal and kinetic rate constants can be calculated per Eqs. (25)–(28). The aqueous Fe(II) concentration at time t is C_{tFe}, thereby, C_{0Fe}= 0 mg/L, and C_{eFe} is the highest Fe(II) dissolution at equilibrium. Constants $k_{1Fe(II)}$ (1/min) and $k_{2Fe(II)}$ (L/(mg·min)) are the kinetic rate constants for the pseudo-first-order kinetic and pseudo-second-order kinetic models during the Fe(II) dissolution, respectively.

The Fe(II) dissolution kinetic data were well fitted by the pseudo-second-order kinetic model with a high correlation coefficient (Table S7). Xie and Cwiertny (2012) suggested that the Fe(II) production in the absence of containments was a strong predictor for Cr removal. Liang et al. (2013) also reported that the extent of Se(IV) removal by nZVI can be predicted from its Fe(II) generation rate, and the Fe(II) production without containments was used as a predictive metric of nZVI corrosion (Li et al., 2015). In this study, dissolved Fe(II) could be considered as the Fe(II) production after reacting with containments, and there was still strong positive linear correlations between the pseudo-second-order rate constants of removed Cd(II) and that of released Fe(II) for S-nZVI (R^2 = 0.91) and nZVI (R^2 = 0.97) (Fig. 11(d)). The further study indicated that the dissolved Fe(II) was an effective predictor in the presence of containments.

4 Conclusions

The performance of Cd(II) removal by three Fe-based nanomaterials were systematically compared and the results revealed that sulfidation of nZVI produced nanomaterials with increased Cd(II) removal capacities.

The main conclusions were as follows:

1) The removal efficiency was significantly increased with elevated doses for three types of nanomaterials. Under identical conditions, the removal of Cd(II) by S-nZVI and nFeS were twice or more than that of nZVI.

2) Again, at varied initial pH, Cd(II) removal by three materials followed the order of S-nZVI > nFeS > nZVI. Higher Cd(II) removal was achieved at higher pH. The pseudo-second-order kinetic model could better fit the removal kinetic data than the pseudo-first-order model. The fast initial reaction rate of nZVI did not lead to a high removal capacity and release of Cd(II) was observed.

3) Though the co-existing ions influenced the performance of nanomaterials differently, the Cd(II) removal by three Fe-nanomaterials were comparable or even slightly enhanced. Notably, the addition of CO_3^{2-} and NO_3^- can influence the properties of Cd(II) and nanomaterials. The addition of HA enhanced the immobilization of Cd(II) mainly due to improved surface complexation of both Fe(II) and Cd(II).

4) The samples before and after reactions were thoroughly examined to compare the Cd removal mechanisms. The reaction mechanisms for Cd removal by nZVI included coprecipitation, surface complexation, and reduction. While for sulfidated materials, the mechanisms involved replacement, coprecipitation, and surface complexation, with the replacement as the predominant reaction.

5) There existed a strong linear correlation between Cd(II) removal and Fe(II) dissolution indicating that the Fe(II) release played a crucial role in the Cd(II) sequestration. A novel pseudo-second-order kinetic model was proposed and could adequately simulate the Fe(II) dissolution results.

Acknowledgements Xiao Zhao is grateful for the support by the National Natural Science Foundation of China (No. 51809267) and the Chinese Universities Scientific Fund (No. 109018).

Electronic Supplementary Material Supplementary material is available in the online version of this article at https://doi.org/10.1007/s11783-022-1586-8 and is accessible for authorized users.

References

Abdel Salam M, Owija N Y, Kosa S (2021). Removal of the toxic cadmium ions from aqueous solutions by zero-valent iron nanoparticles. International Journal of Environmental Science and Technology, 18(8): 2391–2404

Bi X, Pan X, Zhou S (2013). Soil security is alarming in China's main grain producing areas. Environmental Science & Technology, 47(14): 7593–7594

Boparai H K, Joseph M, O'Carroll D M (2013). Cadmium (Cd^{2+}) removal by nano zerovalent iron: Surface analysis, effects of solution chemistry and surface complexation modeling. Environmental Science and Pollution Research International, 20(9): 6210–6221

Brigante M, Zanini G, Avena M (2009). Effect of pH, anions and cations on the dissolution kinetics of humic acid particles. Colloids and Surfaces. A, Physicochemical and Engineering Aspects, 347(1−3): 180−186

Cai Z, Zhao X, Duan J, Zhao D, Dang Z, Lin Z (2020). Remediation of soil and groundwater contaminated with organic chemicals using stabilized nanoparticles: Lessons from the past two decades. Frontiers of Environmental Science & Engineering, 14(5): 84

Davis A P, Bhatnagar V (1995). Adsorption of cadmium and humic acid onto hematite. Chemosphere, 30(2): 243–256

Dong D, Nelson Y M, Lion L W, Shuler M L, Ghiorse W C (2000). Adsorption of Pb and Cd onto metal oxides and organic material in natural surface coatings as determined by selective extractions: New evidence for the importance of Mn and Fe oxides. Water Research, 34(2): 427–436

Dong H, Zhang C, Deng J, Jiang Z, Zhang L, Cheng Y, Hou K, Tang L, Zeng G (2018). Factors influencing degradation of trichloroethylene by sulfide-modified nanoscale zero-valent iron in aqueous solution. Water Research, 135: 1–10

Du J, Bao J, Lu C, Werner D (2016). Reductive sequestration of chromate by hierarchical FeS@Fe^0 particles. Water Research, 102: 73–81

Duan J, Ji H, Zhao X, Tian S, Liu X, Liu W, Zhao D (2020). Immobilization of U(VI) by stabilized iron sulfide nanoparticles: Water chemistry effects, mechanisms, and long-term stability. Chemical Engineering Journal, 393: 124692

Fan D, Lan Y, Tratnyek P G, Johnson R L, Filip J, O'Carroll D M, Nunez Garcia A, Agrawal A (2017). Sulfidation of iron-based materials: A review of processes and implications for water treatment and remediation. Environmental Science & Technology, 51(22): 13070–13085

Fu R, Mu N, Guo X, Xu Z, Bi D (2015). Removal of decabromodiphenyl ether (BDE-209) by sepiolite-supported nanoscale zerovalent iron. Frontiers of Environmental Science & Engineering, 9(5): 867–878

Gong Y, Gai L, Tang J, Fu J, Wang Q, Zeng E Y (2017). Reduction of Cr(VI) in simulated groundwater by FeS-coated iron magnetic nanoparticles. Science of the Total Environment, 595: 743–751

He F, Li Z, Shi S, Xu W, Sheng H, Gu Y, Jiang Y, Xi B (2018). Dechlorination of excess trichloroethene by bimetallic and sulfidated nanoscale zero-valent iron. Environmental Science & Technology, 52(15): 8627–8637

He F, Zhao D (2007). Manipulating the size and dispersibility of zerovalent iron nanoparticles by use of carboxymethyl cellulose stabilizers. Environmental Science & Technology, 41(17): 6216–6221

He F, Zhao D, Liu J, Roberts C B (2007). Stabilization of Fe−Pd nanoparticles with sodium carboxymethyl cellulose for enhanced transport and dechlorination of trichloroethylene in soil and groundwater. Industrial & Engineering Chemistry Research, 46(1): 29–34

Hou C, Zhao J, Zhang Y, Qian Y, Chen J, Yang M, Du J, Chen T, Huang B, Zhou X (2022). Enhanced simultaneous removal of cadmium, lead, and acetochlor in hyporheic zones with calcium

peroxide coupled with zero-valent iron: Mechanisms and application. Chemical Engineering Journal, 427: 130900

Huang J, Yin W, Li P, Bu H, Lv S, Fang Z, Yan M, Wu J (2020). Nitrate mediated biotic zero valent iron corrosion for enhanced Cd(II) removal. Science of the Total Environment, 744: 140715

Huang P, Ye Z, Xie W, Chen Q, Li J, Xu Z, Yao M (2013). Rapid magnetic removal of aqueous heavy metals and their relevant mechanisms using nanoscale zero valent iron (nZVI) particles. Water Research, 47(12): 4050–4058

Hyun S P, Kim B A, Son S, Kwon K D, Kim E, Hayes K F (2021). Cadmium(II) removal by mackinawite under anoxic conditions. ACS Earth & Space Chemistry, 5(6): 1306–1315

Jeong H Y, Han Y S, Park S W, Hayes K F (2010). Aerobic oxidation of mackinawite (FeS) and its environmental implication for arsenic mobilization. Geochimica et Cosmochimica Acta, 74(11): 3182–3198

Kim E J, Murugesan K, Kim J H, Tratnyek P G, Chang Y S (2013). Remediation of trichloroethylene by FeS-coated iron nanoparticles in simulated and real groundwater: Effects of water chemistry. Industrial & Engineering Chemistry Research, 52(27): 9343–9350

Lee H, Lee H J, Kim H E, Kweon J, Lee B D, Lee C (2014). Oxidant production from corrosion of nano- and microparticulate zero-valent iron in the presence of oxygen: a comparative study. Journal of Hazardous Materials, 265: 201–207

Li J, Qin H, Guan X (2015). Premagnetization for enhancing the reactivity of multiple zerovalent iron samples toward various contaminants. Environmental Science & Technology, 49(24): 14401–14408

Li X Q, Zhang W X (2007). Sequestration of metal cations with zerovalent iron nanoparticles–A study with high resolution X-ray photoelectron spectroscopy (HR-XPS). Journal of Physical Chemistry C, 111(19): 6939–6946

Li J, Zhang X, Sun Y, Liang L, Pan B, Zhang W, Guan X (2017). Advances in sulfidation of zerovalent iron for water decontamination. Environmental Science & Technology, 51(23): 13533–13544

Li Y H, Wang S, Luan Z, Ding J, Xu C, Wu D (2003). Adsorption of cadmium(II) from aqueous solution by surface oxidized carbon nanotubes. Carbon, 41(5): 1057–1062

Liang L, Li W, Li Y, Zhou W, Chen J (2021a). Removal of EDTA-chelated CdII by sulfidated nanoscale zero-valent iron: Removal mechanisms and influencing factors. Separation and Purification Technology, 276: 119332

Liang L, Li X, Guo Y, Lin Z, Su X, Liu B (2021b). The removal of heavy metal cations by sulfidated nanoscale zero-valent iron (S-nZVI): The reaction mechanisms and the role of sulfur. Journal of Hazardous Materials, 404(Pt A): 124057

Liang L, Li X, Lin Z, Tian C, Guo Y (2020). The removal of Cd by sulfidated nanoscale zero-valent iron: the structural, chemical bonding evolution and the reaction kinetics. Chemical Engineering Journal, 382: 122933

Liang L, Yang W, Guan X, Li J, Xu Z, Wu J, Huang Y, Zhang X (2013). Kinetics and mechanisms of pH-dependent selenite removal by zero valent iron. Water Research, 47(15): 5846–5855

Ling L, Huang X, Li M, Zhang W X (2017). Mapping the reactions in a single zero-valent iron nanoparticle. Environmental Science & Technology, 51(24): 14293–14300

Liu B, Hu K, Jiang Z, Qu F, Su X (2011). A 50-year sedimentary record of heavy metals and their chemical speciations in the Shuangtaizi River estuary (China): implications for pollution and biodegradation. Frontiers of Environmental Science & Engineering in China, 5(3): 435–444

Lv D, Zhou X, Zhou J, Liu Y, Li Y, Yang K, Lou Z, Baig S A, Wu D, Xu X (2018). Design and characterization of sulfide-modified nanoscale zerovalent iron for cadmium(II) removal from aqueous solutions. Applied Surface Science, 442: 114–123

Ma D, Gao H (2014). Reuse of heavy metal-accumulating Cynondon dactylon in remediation of water contaminated by heavy metals. Frontiers of Environmental Science & Engineering, 8(6): 952–959

Mielczarski J A, Atenas G M, Mielczarski E (2005). Role of iron surface oxidation layers in decomposition of azo-dye water pollutants in weak acidic solutions. Applied Catalysis B: Environmental, 56(4): 289–303

Min Y, Akbulut M, Kristiansen K, Golan Y, Israelachvili J (2008). The role of interparticle and external forces in nanoparticle assembly. Nature Materials, 7(7): 527–538

Mustafa S, Misbahud D, Sammad Y H, Zaman M I, Sadullah K (2010). Sorption mechanism of cadmium from aqueous solution on iron sulphide. Chinese Journal of Chemistry, 28(7): 1153–1158

Naushad M, Ahamad T, Alothman Z A, Shar M A, Alhokbany N S, Alshehri S M (2015). Synthesis, characterization and application of curcumin formaldehyde resin for the removal of Cd^{2+} from wastewater: kinetics, isotherms and thermodynamic studies. Journal of Industrial and Engineering Chemistry, 29: 78–86

Neumann A, Sander M, Hofstetter T B (2011). Chapter 17: Redox Properties of Structural Fe in Smectite Clay Minerals. In: Tratnyek P, Grundl T, Haderlein S, editors. Aquatic Redox Chemistry. San Francisco: American Chemical Society, 361–379

Phenrat T, Saleh N, Sirk K, Tilton R D, Lowry G V (2007). Aggregation and sedimentation of aqueous nanoscale zerovalent iron dispersions. Environmental Science & Technology, 41(1): 284–290

Qiao J T, Liu T X, Wang X Q, Li F B, Lv Y H, Cui J H, Zeng X D, Yuan Y Z, Liu C P (2018). Simultaneous alleviation of cadmium and arsenic accumulation in rice by applying zero-valent iron and biochar to contaminated paddy soils. Chemosphere, 195: 260–271

Rajajayavel S R, Ghoshal S (2015). Enhanced reductive dechlorination of trichloroethylene by sulfidated nanoscale zerovalent iron. Water Research, 78: 144–153

Reed B E, Matsumoto M R (1993). Modeling cadmium adsorption by activated carbon using the Langmuir and Freundlich isotherm expressions. Separation Science and Technology, 28(13-14): 2179–2195

Su Y, Adeleye A S, Huang Y, Sun X, Dai C, Zhou X, Zhang Y, Keller A A (2014). Simultaneous removal of cadmium and nitrate in aqueous media by nanoscale zerovalent iron (nZVI) and Au doped nZVI particles. Water Research, 63: 102–111

Su Y, Adeleye A S, Keller A A, Huang Y, Dai C, Zhou X, Zhang Y (2015). Magnetic sulfide-modified nanoscale zerovalent iron (S-nZVI) for dissolved metal ion removal. Water Research, 74: 47–57

Sun Y, Li J, Huang T, Guan X (2016). The influences of iron characteristics, operating conditions and solution chemistry on

contaminants removal by zero-valent iron: A review. Water Research, 100: 277–295

Sun Y, Lou Z, Yu J, Zhou X, Lv D, Zhou J, Baig S A, Xu X (2017). Immobilization of mercury (II) from aqueous solution using Al_2O_3-supported nanoscale FeS. Chemical Engineering Journal, 323: 483–491

Thakur A K, Nisola G M, Limjuco L A, Parohinog K J, Torrejos R E C, Shahi V K, Chung W J (2017). Polyethylenimine-modified mesoporous silica adsorbent for simultaneous removal of Cd(II) and Ni(II) from aqueous solution. Journal of Industrial and Engineering Chemistry, 49: 133–144

Tian S, Gong Y, Ji H, Duan J, Zhao D (2020). Efficient removal and long-term sequestration of cadmium from aqueous solution using ferrous sulfide nanoparticles: Performance, mechanisms, and long-term stability. Science of the Total Environment, 704: 135402

Touomo-Wouafo M, Donkeng-Dazie J, Btatkeu-K B D, Tchatchueng J B, Noubactep C, Ludvík J (2018). Role of pre-corrosion of Fe^0 on its efficiency in remediation systems: An electrochemical study. Chemosphere, 209: 617–622

Turcio-Ortega D, Fan D, Tratnyek P G, Kim E J, Chang Y S (2012). Reactivity of Fe/FeS nanoparticles: electrolyte composition effects on corrosion electrochemistry. Environmental Science & Technology, 46(22): 12484–12492

Wang Q, Wang S, Liu M (2004). Safety evaluation on pollution of xiang river valley in hunan province. Zhongguo Jishui Paishui, 20: 104-106 (in Chinese)

WHO (2004). Background document for development of WHO guidelines for drinking-water quality and guidelines for safe recreational water environments. Geneva: World Health Organisation

Wu L, Yu J C, Fu X Z (2006). Characterization and photocatalytic mechanism of nanosized CdS coupled TiO_2 nanocrystals under visible light irradiation. Journal of Molecular Catalysis, A-Chemical, 244(1–2): 25–32

Xie Y, Cwiertny D M (2012). Influence of anionic cosolutes and pH on nanoscale zerovalent iron longevity: Time scales and mechanisms of reactivity loss toward 1,1,1,2-tetrachloroethane and Cr(VI). Environmental Science & Technology, 46(15): 8365–8373

Xu H, Sun Y, Li J, Li F, Guan X (2016). Aging of zerovalent iron in synthetic groundwater: X-ray photoelectron spectroscopy depth profiling characterization and depassivation with uniform magnetic field. Environmental Science & Technology, 50(15): 8214–8222

Yamashita T, Hayes P (2008). Analysis of XPS spectra of Fe^{2+} and Fe^{3+} ions in oxide materials. Applied Surface Science, 254(8): 2441–2449

Zhang C, Li Y, Wang T J, Jiang Y, Wang H (2016a). Adsorption of drinking water fluoride on a micron-sized magnetic Fe_3O_4@Fe-Ti composite adsorbent. Applied Surface Science, 363: 507–515

Zhang Q, Guo W, Yue X, Liu Z, Li X (2016b). Degradation of rhodamine B using FeS-coated zero-valent iron nanoparticles in the presence of dissolved oxygen. Environmental Progress & Sustainable Energy, 35(6): 1673–1678

Zhang Y, Li Y, Dai C, Zhou X, Zhang W (2014). Sequestration of Cd(II) with nanoscale zero-valent iron (nZVI): Characterization and test in a two-stage system. Chemical Engineering Journal, 244: 218–226

Zhao X, Liu W, Cai Z, Han B, Qian T, Zhao D (2016). An overview of preparation and applications of stabilized zero-valent iron nanoparticles for soil and groundwater remediation. Water Research, 100: 245–266